IEEE Access
Multidisciplinary | Rapid Review | Open Access Journal

IEEE PHOTONICS SOCIETY SECTION

Received 24 July 2025, accepted 2 September 2025, date of publication 5 September 2025, date of current version 12 September 2025.

Digital Object Identifier 10.1109/ACCESS.2025.3606842

RESEARCH ARTICLE

Wavelength-Selective Coupling to Vertical Higher Order Modes in a 500-nm-Thick Silicon Multimode Waveguide Using Long- and Short-Period Gratings

HYEONGJUNG KIM, JUNGWOO LEE, JIHOON SEO, MINJIN KIM, AND MIN-SUK KWON
Department of Electrical Engineering, Ulsan National Institute of Science and Technology, Ulsan 44919, South Korea

Corresponding author: Min-Suk Kwon (mskwon@unist.ac.kr)

This work was supported by the Challengeable Future Defense Technology Research and Development Program through the ADD funded by DAPA, in 2024, under Grant UI220080TD.

ABSTRACT This work explores thick silicon multimode waveguides (MMWs), focusing on vertical multimode operation. We present grating-assisted coupling structures to efficiently convert the fundamental mode to vertical higher-order modes in a 500-nm-thick silicon MMW. Both forward and backward coupling schemes are investigated. The forward coupling with a long-period grating exhibits broadband conversion over a coupling length less than 40μm. The backward coupling with a short-period grating demonstrates mode conversion with a 3-dB bandwidth ranging from 5.8 to 13.3 nm. These results open new avenues for applications such as on-chip spatial mode multiplexing with a higher capacity.

INDEX TERMS Integrated optics, silicon photonics, multimode waveguides, Bragg gratings, notch filters.

I. INTRODUCTION

Silicon (Si) photonics is flourishing to meet the insatiable data demands of AI and quantum computing [1], [2]. While single-mode waveguides (SMWs) have been the predominant choice for photonic integrated circuits (PICs), multimode waveguides (MMWs) offer several advantages [3]. MMWs exhibit lower propagation loss for the fundamental transverse electric (TE) mode (TE_{00} mode), leading to improved performance in delay lines [4]. Furthermore, the propagation constant of the TE_{00} mode in MMWs is less susceptible to fabrication variations, making them suitable for devices requiring precise phase control [5]. Notably, MMWs support horizontal higher-order modes (TE_{i0} modes, $i \geq 1$), enabling enhanced functionalities such as on-chip mode division multiplexing (MDM) [6], [7], [8], non-resonant multi-pass structures [9], [10], and modal phase-matching for nonlinear optical interactions [11].

The associate editor coordinating the review of this manuscript and approving it for publication was Leo Spiekman.

The standard Si thickness of Si-on-insulator (SOI) wafers processed in foundries is 220 nm [12], restricting MMWs to horizontal multimode operation. Increasing the Si thickness above 220 nm enables vertical multimode operation, significantly expanding the available mode space. For example, 500-nm-thick Si strip MMWs support TE_{i1} modes as well as TE_{i0} modes. This increased mode availability could double the capacity of on-chip MDM systems, provided that efficient mode converters and (de)multiplexers for TE_{i1} modes are developed. Furthermore, a notable advantage of TE_{i1} modes is their potential for direct conversion from certain linearly polarized (LP) modes in few-mode fibers via grating couplers, eliminating the need for additional on-chip structures [13]. While SOI wafers with 500-nm-thick silicon layers have been utilized in mid-infrared photonic devices [14], [15] and active devices based on hybrid III-V semiconductor integration [16], [17], manipulating and exploiting multiple modes in such MMWs has remained largely unexplored.

In this work, we present grating-assisted coupling structures to efficiently convert the TE_{00} mode to vertical higher-order TE modes (TE_{01} and TE_{11}) in a

500-nm-thick, 1.2-μm-wide Si MMW. Both forward (co-directional) and backward (contra-directional) coupling schemes are investigated for the wavelength-selective mode conversion, employing long-period and short-period gratings, respectively. Despite a modest number of grating periods (only 10), the forward coupling effectively generates a broad rejection band with an extinction ratio exceeding 10 dB in the TE_{00} mode transmission spectrum. The backward coupling generates a rejection band characterized by an extinction ratio greater than 10 dB and a 3-dB bandwidth of 5.8 to 13.3 nm. These findings demonstrate the potential of leveraging vertical multimode operation in MMWs for applications such as on-chip MDM with a higher capacity and on-chip processing of a few-mode fiber's LP modes.

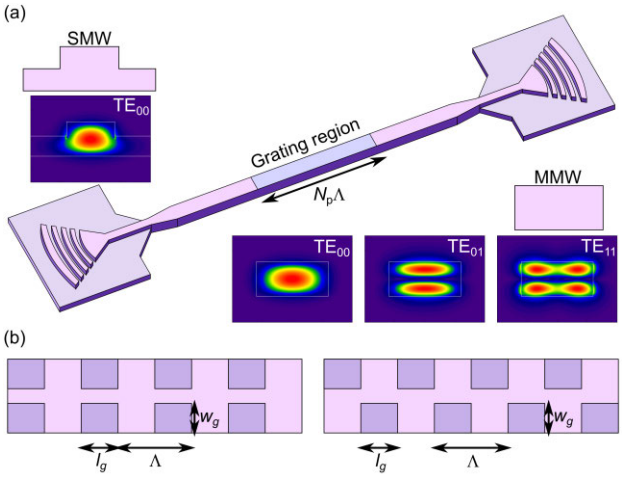

FIGURE 1. (a) Schematic of the photonic integrated circuit with grating-assisted coupling (PICGAC). The electric field magnitude profile of the TE_{00} mode of the single-mode rib waveguide is shown in the left top region. Those of the TE_{00}, TE_{01}, and TE_{11} modes of the multimode strip waveguide are shown in the right bottom region. (b) Grating structures. The left and right structures are used for the coupling from the TE_{00} mode to the TE_{01} and TE_{11} modes, respectively.

II. DEVICE STRUCTURE AND FABRICATION

The investigated PIC with grating-assisted coupling (PICGAC) consists of input and output single-mode rib waveguides, a multimode strip waveguide with a grating on its top surface, and couplers between the SMW and the MMW (Fig. 1(a)). This grating utilizes a shallow Si etch process, which contrasts with the width-modulated gratings typically employed in 220-nm-thick Si MMWs [18], [19], [20]. The shallow-etched surface grating offers several notable advantages over width-modulated alternatives: it provides an additional degree of freedom in grating design, enables the simultaneous use of both surface and sidewall gratings for applications such as sensing, and generally leads to easier fabrication (see Appendix A for further details). The designed SMWs comprise an 800-nm-wide, 230-nm-high rib and a 270-nm-thick slab. The grating for coupling between the TE_{00} and TE_{01} (TE_{11}) modes is formed by periodically etching pairs of two transversely parallel (diagonally positioned) rectangles with an area of $w_g \times l_g$ by a depth of 40 nm (Fig. 1(b)). The grating period and number of periods are denoted by Λ and N_p, respectively, and $N_p \times \Lambda$ is equal to a grating length or coupling length (L). The couplers transform the TE_{00} mode of the SMW into the TE_{00} mode of the MMW and vice versa. Within the coupler, the slab width transitions from 4 μm to 800 nm over a distance of 7 μm, followed by a transition of the Si strip width from 800 nm to 1.2 μm over a distance of 8 μm. The SMWs are connected to focusing grating couplers, which are formed by etching grating arcs of width 268 nm by a depth of 230 nm. The period of the arcs is 536 nm. We denote the PICGACs for coupling to the TE_{01} and TE_{11} modes as PICGAC0 and PICGAC1, respectively.

The values of w_g, l_g, Λ and N_p were determined for efficient coupling at a desired wavelength (λ_c). For a given value of w_g, l_g was initially calculated using the formula $l_g = \lambda_c/[2(n'_{00} \mp n'_{i1})]$, where n'_{00} and n'_{i1} represent the effective indices of the TE_{00} and TE_{i1} modes in the shallowly etched waveguide section, with the minus and plus signs corresponding to the forward and backward coupling, respectively. For the PICGAC0, Λ was set to $l_g + \lambda_c/[2(n_{00} \mp n_{i1})]$, where n_{00} and n_{i1} represent the effective indices of the TE_{00} and TE_{i1} modes in the unetched waveguide section, respectively. For the PICGAC1, Λ was defined as $2l_g$. Subsequently, the values of l_g and Λ were refined using the eigenmode expansion (EME) solver in Lumerical MODE to maximize the transmittance from the TE_{00} mode to the TE_{i1} mode at λ_c (see Appendix B for simulation details). Finally, N_p was determined to achieve a peak in the forward-coupling transmittance while ensuring the backward-coupling transmittance exceeds 0.95.

Fig. 2 illustrates the calculated relationships between N_p and w_g for $\lambda_c = 1550$ nm. Additionally, the full width at half maximum (FWHM) of the transmittance spectrum from the TE_{00} mode to the TE_{i1} mode was calculated, and its relationships with w_g are also depicted in the same figure. As w_g increases, the spatial overlap between the TE_{00} and TE_{i1} modes within the etched region increases, leading to an exponential decrease in N_p. This trend is supported by the exponentially decaying curves fitted to the numerically obtained N_p versus w_g data. Notably, for the PICGAC1, N_p remains constant when w_g is between 500 nm and 600 nm. This behavior arises because the electric field profile of the TE_{11} mode has a node along the central vertical line. Finally, the calculated relationship between the FWHM and w_g is compared against theoretical curves derived from the expression:

$$\mathrm{FWHM} = C\frac{\lambda_c}{N_p}\left|\Lambda\left(\frac{dn_{00}}{d\lambda} \mp \frac{dn_{i1}}{d\lambda}\right) - 1\right|^{-1}. \quad (1)$$

For forward coupling, the constant C is 0.7987, and the negative sign is applied in (1). Conversely, for backward coupling, C is 1.901, and the positive sign is used (refer to Appendix C for details). The numerically obtained relationships show good agreement with the theoretical predictions. The results presented in Fig. 2 suggest that forward coupling

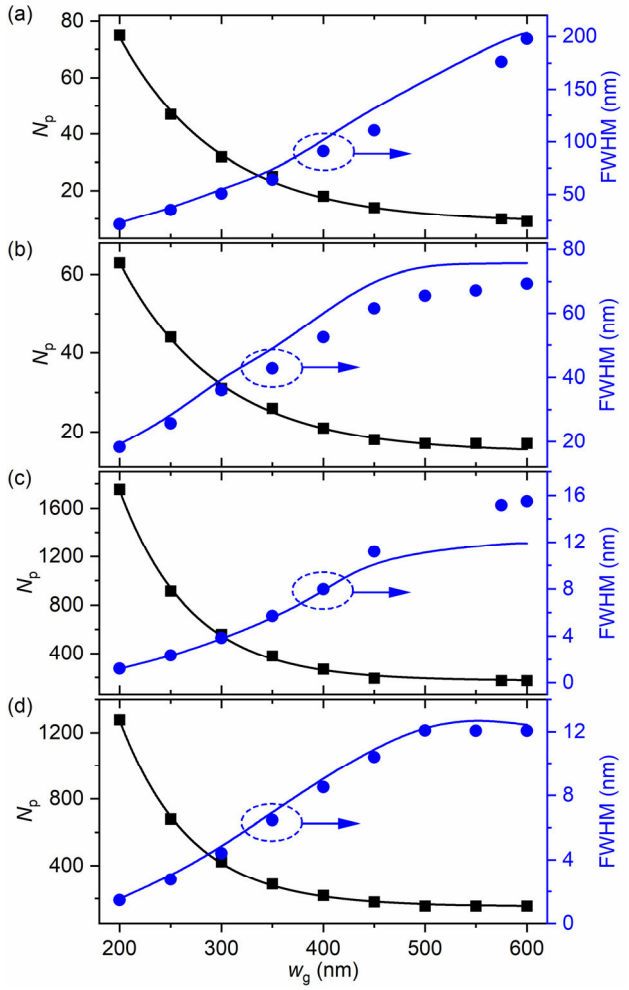

FIGURE 2. Relationships between the number of grating periods (N_p) and the etched region width (w_g) (black squares), and the full width at half maximum (FWHM) of the transmittance spectrum to the TE_{i1} mode as a function of w_g (blue circles). Panels (a) and (b) show the forward coupling characteristics to the TE_{01} mode in the PICGAC0 (a) and to the TE_{11} mode in the PICGAC1 (b). Panels (c) and (d) illustrate the backward coupling characteristics to the TE_{01} mode in PICGAC0 (c) and to the TE_{11} mode in PICGAC1 (d). The black solid lines represent exponential decay fits to the numerically calculated N_p versus w_g data. The blue solid lines are generated using the analytic expression for the FWHM given in (1).

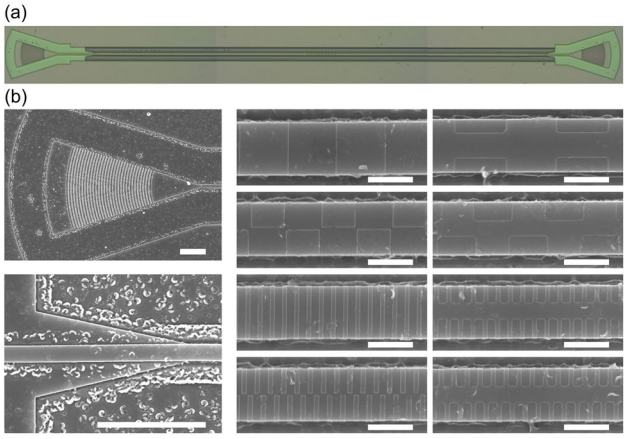

FIGURE 3. (a) Optical microscope image of the fabricated PICGAC. (b) SEM images of fabricated PICGAC parts. The left panels show the grating coupler and coupler between the rib and strip waveguides. The right panels show the grating regions. The top two rows illustrate forward coupling gratings for PICGAC0 and PICGAC1, respectively, while the bottom two rows display backward coupling gratings for the same. Debris remains on the Si patterns due to the removal of the Si oxide cladding for the SEM observation. Scale bars: 5 μm (left panels), 1 μm (right panels).

is well-suited for broadband excitation of the TE_{01} or TE_{11} mode over short interaction lengths. In contrast, backward coupling is more appropriate for narrowband excitation. For instance, at $w_g = 600$ nm, the forward coupling to the TE_{01} mode yields an FWHM of 198 nm with a grating length of 19.8 μm (corresponding to $\Lambda = 2.20$ μm and $N_p = 9$). However, when w_g is reduced to 200 nm, the backward coupling to the TE_{11} mode can achieve a narrow FWHM of 1.54 nm over a longer grating length of 364 μm ($\Lambda = 0.284$ μm and $N_p = 1280$). For grating lengths shorter than 100 μm, PICGAC0 and PICGAC1 structures with w_g ranging from 300 nm to 600 nm were experimentally studied.

The PICGACs were fabricated using a foundry service (NanoSOI Fabrication Service, Applied Nanotools Inc.). The SOI wafer employed features a 500-nm-thick Si layer and a 1-μm-thick buried oxide (the exact Si thickness is 496 nm). To pattern the gratings, rib waveguides, and strip waveguides, three successive e-beam lithography steps were executed. As a result of slight Si over-etching, the fabricated rib height and grating coupler arc depth are 247 nm, while the grating etch depth measures 45 nm. An optical microscope image of the fabricated PICGAC is shown in Fig. 3(a), and representative scanning electron microscope (SEM) images of its SMW, MMW, grating coupler, and gratings are depicted in Fig. 3(b). The transmission spectra of the PICGACs were characterized using a tunable laser with a wavelength resolution of 1 nm and an optical power meter. These spectra were normalized to the transmission spectrum of a 300-μm-long SMW connected to the grating couplers. To remove noise during the characterization, the forward-coupling transmission spectra were smoothed with a fast Fourier transform filter. At a wavelength of 1550 nm, the grating couplers exhibit a coupling loss of 8 dB, while the propagation loss of the SMW is 1.5 dB/cm.

III. FORWARD COUPLING WITH LONG-PERIOD GRATINGS

The PICGAC0 (Photonic Integrated Circuit using Grating-Assisted Coupling to the TE_{01} mode) with dimensions (w_g, l_g, Λ) = (600 nm, 0.997 μm, 2.14 μm) exhibits a rejection band centered at approximately 1533 nm, resulting from the forward coupling between the TE_{00} and TE_{01} modes (Fig. 4(a)). The extinction ratio of this rejection band increases with the number of grating periods, N_p. For $N_p = 10$, an extinction ratio of 24.5 dB is achieved. The PICGAC0 with (w_g, l_g, Λ) = (300 nm, 1.093 μm, 2.24 μm) displays a rejection band centered at approximately 1530 nm (Fig. 4(b)). Due to the inherent nature of forward coupling, the extinction ratio of this rejection band initially increases with N_p but subsequently decreases as N_p increases beyond 30 and up to 36.

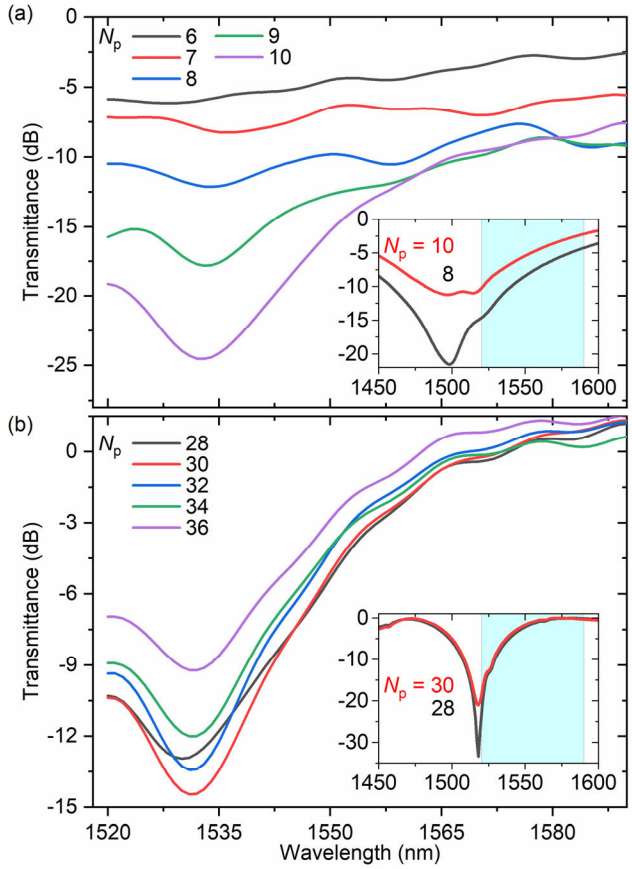

FIGURE 4. (a), (b) Measured transmission spectra of the PICGAC0 with w_g = (a) 600 nm and (b) 300 nm. The rejection bands are attributed to the forward coupling between the TE_{00} and TE_{01} modes. The insets present the calculated transmission spectra of the PICGAC0. The cyan colored regions correspond to the measurement wavelength range.

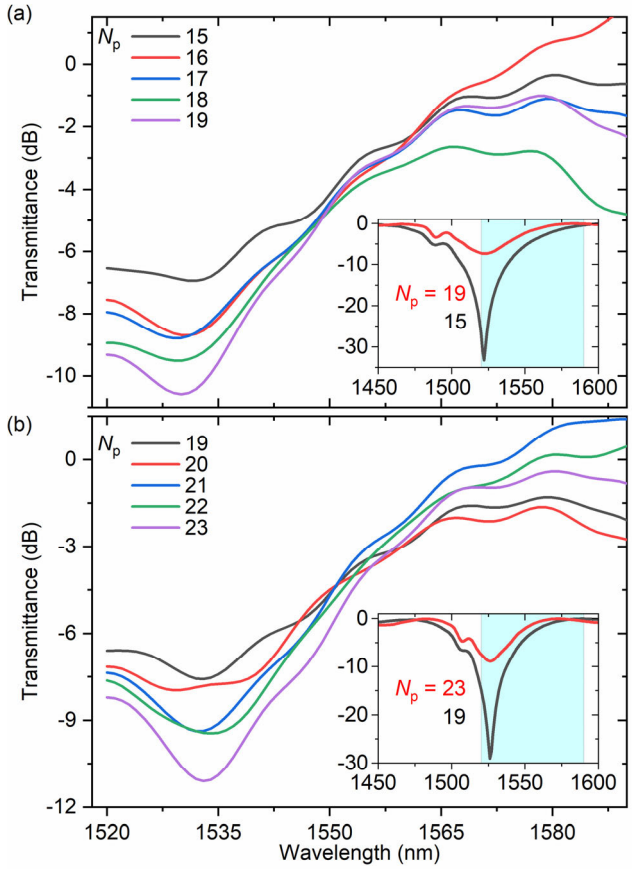

FIGURE 5. (a), (b) Measured transmission spectra of the PICGAC1 with w_g = (a) 600 nm and (b) 400 nm. The rejection bands are attributed to the forward coupling between the TE_{00} and TE_{11} modes. The insets present the calculated transmission spectra of the PICGAC0. The cyan colored regions correspond to the measurement wavelength range.

As shown in Fig. 2(a), the reduction in w_g from 600 nm to 300 nm leads to an increase in N_p. Consequently, the PICGAC0 with $w_g = 300$ nm requires a larger N_p value to achieve maximum extinction ratio compared to the one with $w_g = 600$ nm. Furthermore, the rejection bands for $w_g = 300$ nm are observed to be sharper than those for $w_g = 600$ nm. This increased sharpness aligns with the trend of decreasing FWHM for smaller w_g, as illustrated in Fig. 2(a). The observed center wavelengths are shorter than the 1550 nm design target due to fabrication discrepancies; the actual Si thickness and grating depth differ from the design values. Numerical simulations incorporating these realized parameters confirm this, predicting center wavelengths of 1498 nm ($w_g = 600$ nm) and 1518 nm ($w_g = 300$ nm), respectively (see insets). They exhibit maximum extinction ratios at N_p values of 8 and 28, respectively. This discrepancy between the calculated and measured N_p values for maximum extinction ratio suggests that the actual coupling strengths in the realized PICGAC0s are lower than predicted. Additionally, the calculated rejection band for $w_g = 600$ nm is significantly broad, explaining the observed low transmittance in the wavelength range of 1520 nm to 1590 nm.

The transmission spectra of the PICGAC1s (Photonic Integrated Circuits using Grating-Assisted Coupling to the TE_{11} mode) with dimensions (w_g, l_g, Λ) = (600 nm, 0.7805 μm, 1.561 μm) and (400 nm, 0.7873 μm, 1.5746 μm) are presented in Fig. 5. The rejection bands observed in these spectra are attributed to the forward coupling between the TE_{00} and TE_{11} modes. As N_p increases, the extinction ratio of the rejection band also increases. For $w_g = 600$ nm and 400 nm, the maximum extinction ratios achieved are 10.6 dB at 1530 nm for $N_p = 19$ and 11.1 dB at 1533 nm for $N_p = 23$, respectively. Notably, Fig. 2(b) shows that both N_p and the FWHM change slightly as w_g decreases from 600 nm down to 400 nm. This small change, attributed to the electric field profile of the TE_{11} mode, is confirmed by our experimental results. As illustrated in the insets, numerical simulations of the realized devices reveal that the calculated transmission spectra exhibit rejection bands with maximum extinction ratios at $N_p = 15$ and 19 for $w_g = 600$ nm and 400 nm, respectively. Consistent with the findings for the PICGAC0s, the realized PICGAC1s demonstrate coupling strengths that are lower than those predicted by the simulations. Figs. 4 and 5 verify the capability of the PICGACs to provide broadband

forward coupling into the TE_{01} or TE_{11} mode within a short interaction length.

The coupling coefficients (κ) between the TE_{00} and TE_{01} modes, and between the TE_{00} and TE_{11} modes, were determined from the measured minimum transmittances (T_{min}) using the relationship: $\kappa = \cos^{-1}\left(\sqrt{T_{min}}\right)/L$, where $L = N_p \cdot \Lambda$. Table 1 summarizes both the experimentally derived and theoretically calculated values of κ. The observed dependence of κ on w_g and the difference between experimental and theoretical values provide a quantitative explanation for the observed features in the transmission spectra of Figs. 4 and 5.

For comparison, a previously reported grating-assisted co-directional coupler based on a 230-nm-thick and 1-μm-wide Si waveguide, designed for coupling between the TE_{00} and TE_{10} modes, achieved a rejection band with an extinction ratio of 13 dB over a grating length of 260 μm, utilizing 5-nm width modulations on each waveguide sidewall [21]. In contrast, the PICGACs demonstrate significantly shorter coupling lengths for comparable mode conversion efficiencies. This direct comparison highlights that the shallow-etched surface gratings employed in our PICGACs yield substantially higher coupling strengths.

IV. BACKWARD COUPLING WITH SHORT-PERIOD GRATINGS

In contrast to the forward coupling to the TE_{01} or TE_{11} mode, the backward coupling can generate a relatively narrow rejection band in the transmission spectrum of the PICGAC. This phenomenon is evident in the measured transmission spectra of the PICGAC0s with (w_g, N_p) = (600 nm, 300) and (400 nm, 360), as depicted in Fig. 6(a). For w_g = 600 nm, the (l_g, Λ) parameters are (136 nm, 270 nm), (138 nm, 274 nm), and (140 nm, 278 nm). Similarly, for w_g = 400 nm, (l_g, Λ) is (135 nm, 268 nm), (137 nm, 272 nm), and (139 nm, 276 nm). The rejection band arising from the backward coupling between the TE_{00} and TE_{01} modes exhibits a redshift as Λ increases. The average 3-dB bandwidths of the rejection bands are measured to be 13.3 nm and 5.8 nm for w_g = 600 nm and 400 nm, respectively. According to the simulations shown in Fig. 2(c), achieving a theoretical cross-over transmittance to the TE_{01} mode of ≥ 0.95 requires N_p values of 175 (for w_g = 600 nm) and 270 (for w_g = 400 nm). However, the experimental N_p values employed exceed these theoretical predictions by factors of 1.71 and 1.33 for w_g = 600 nm and 400 nm, respectively. Consequently, the rejection bands for w_g = 600 nm exhibit larger extinction ratios compared to those for w_g = 400 nm. The measured spectra closely resemble the calculated spectra shown in Fig. 6(b), although the experimental extinction ratios and bandwidths are slightly smaller than the predicted values. These discrepancies suggest that the coupling strengths in the realized PICGAC0s are lower than those calculated, a trend consistent with the observations made for the forward coupling.

To investigate the backward coupling between the TE_{00} and TE_{11} modes, the PICGAC1s with (w_g, N_p) = (600 nm, 300) and (400 nm, 360) were fabricated and measured

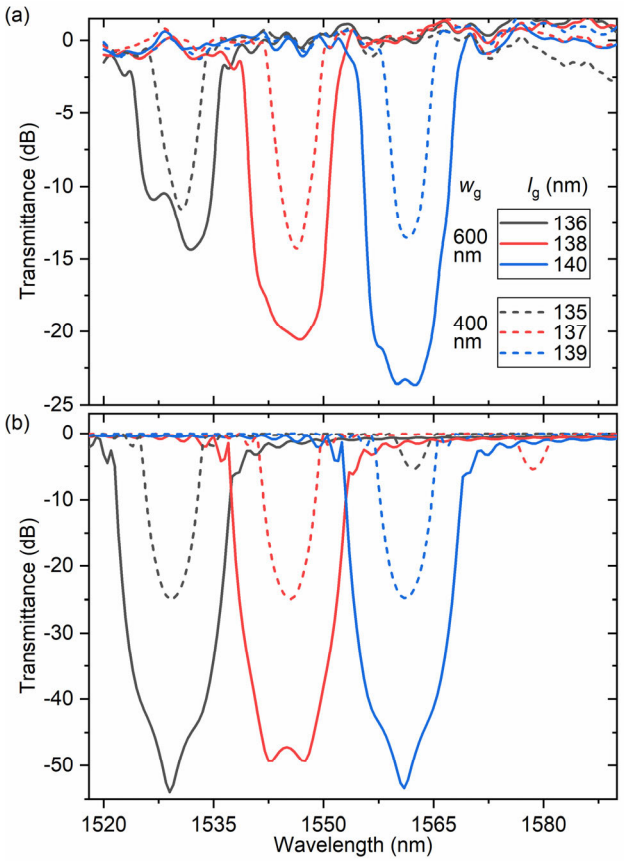

FIGURE 6. (a) Measured transmission spectra of the PICGAC0 in the case of the backward coupling between TE_{00} and TE_{01} modes. (b) Calculated transmission spectra corresponding to those in (a). The solid and dashed curves show the transmission spectra for w_g = 600 nm and 400 nm, respectively.

(Fig. 7(a)). The l_g values for the PICGAC1s with w_g = 600 nm are 142 nm, 144 nm, and 146 nm, while those with w_g = 400 nm were 141 nm, 143 nm, and 145 nm. The transmission spectra of the PICGAC1s exhibit similar features to those observed in Fig. 6(a): a redshift of the rejection band with increasing Λ and larger extinction ratios and bandwidths for w_g = 600 nm compared to w_g = 400 nm. The average 3-dB bandwidths are measured to be 9.4 nm and 7.1 nm for w_g = 600 nm and 400 nm, respectively. However, the differences in extinction ratios and bandwidths between w_g = 600 nm and 400 nm are less pronounced compared to those observed in Fig. 6. This is consistent with the smaller difference in the N_p values for a cross-over transmittance exceeding 0.95 to the TE_{11}mode, which are 155 and 220 for w_g = 600 nm and 400 nm, respectively (Fig. 2(d)). The calculated transmission spectra presented in Fig. 7(b) are qualitatively consistent with the measured spectra. However, due to the fact that the coupling strengths found in the calculations are larger than those in the realized PICGAC1s, the calculated rejection bands exhibit larger extinction ratios and bandwidths compared to the measured rejection bands.

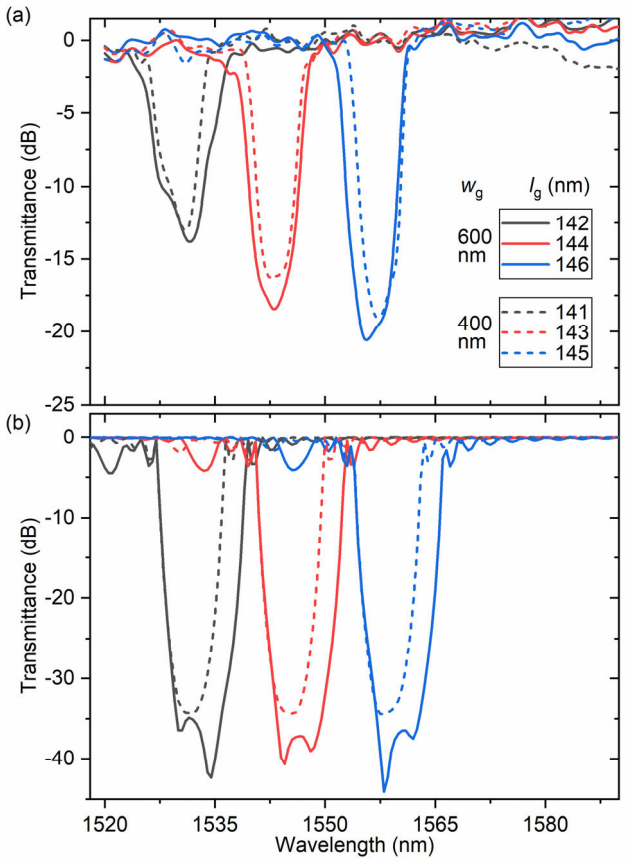

FIGURE 7. (a) Measured transmission spectra of the PICGAC1 in the case of the backward coupling between TE_{00} and TE_{11} modes. (b) Calculated transmission spectra corresponding to those in (a). The solid and dashed curves show the transmission spectra for $w_g = 600$ nm and 400 nm, respectively.

Figs. 6 and 7 illustrate that the transmittances at wavelengths outside the rejection bands are approximately 0 dB. This indicates that the insertion losses of the PICGACs are significantly small. Furthermore, these figures provide experimental validation, demonstrating that the PICGACs, utilizing backward coupling, effectively enable narrow-band excitation of the TE_{01} and TE_{11} modes.

The coupling coefficients (κ) for these backward coupling mechanisms were determined from the measured minimum transmittances (T_{min}) using the following equation: $\kappa = \text{sech}^{-1}\left(\sqrt{T_{min}}\right)/L$, where $L = N_p \cdot \Lambda$. Both the experimental and theoretical values of κ are summarized in Table 1. We observed that the discrepancies between the experimental and theoretical values for the backward couplings are more pronounced than those for the forward couplings. This divergence likely stems from non-ideal grating geometries, as evidenced by the SEM images in Fig. 3(b), which show that the actual l_g values are larger than their design specifications.

For comparison, a previously reported grating-assisted contra-directional coupler, designed for TE_{00} and TE_{10} mode coupling in a 220-nm-thick and 1.2-μm-wide Si waveguide, achieved a 35 dB extinction ratio over a 500-μm grating length using 100-nm waveguide sidewall width modulations [18]. Notably, this grating length is approximately five times larger than those employed in our PICGACs. Consequently, our PICGACs exhibit higher coupling strengths compared to this reported device.

TABLE 1. Experimental and theoretical coupling coefficients.

Type[a]	Mode[b]	w_g (nm)	Λ (μm)	N_p	L (μm)	κ (mm^{-1}) Exp.	Sim.
F	TE_{01}	600	2.14	10	21.4	70.6	86.8
F	TE_{01}	300	2.24	30	67.2	20.6	24.7
F	TE_{11}	600	1.561	19	29.7	42.8	66.1
F	TE_{11}	400	1.575	23	36.2	35.6	51.3
B	TE_{01}	600	0.274	300	82.2	37.4	74.5
B	TE_{01}	400	0.272	360	97.9	24.0	36.0
B	TE_{11}	600	0.288	300	86.4	33.0	57.6
B	TE_{11}	400	0.286	360	103	25.1	45.1

[a]F: forward coupling, B: backward coupling
[b]Mode coupled to the TE_{00} mode

V. CONCLUSION

This work has successfully demonstrated the coupling of the TE_{00} mode to the TE_{01} and TE_{11} modes in 500-nm-high Si multimode waveguides (MMWs) using both long- and short-period gratings. The forward and backward couplings to the vertical higher-order modes are explored, resulting in rejection bands in the transmission spectrum of the TE_{00} mode. The broad rejection bands observed in the case of the forward coupling highlight the efficient conversion of the TE_{00} mode to the TE_{01} or TE_{11} modes over a wide wavelength range using relatively short coupling regions. In contrast, the narrow rejection bands achieved with the backward coupling, typically less than 14 nm in 3-dB bandwidth, make it suitable for mode conversion within a specific wavelength range. Our experimental and theoretical results have shown that the bandwidth of the rejection bands can be effectively controlled by adjusting the etched region width (w_g).

To directly verify the presence of the converted TE_{01} and TE_{11} modes and, furthermore, realize a mode division multiplexing (MDM) system based on 500-nm-thick Si strip MMWs, mode (de)multiplexers such as adiabatic mode couplers capable of extracting them from the MMWs are required. Developing efficient mode (de)multiplexers for higher-order modes such as TE_{01} and TE_{11} modes typically involves complex designs that can occupy a substantial on-chip footprint. However, inverse-designed structures could offer a promising pathway to mitigate this problem [22]. Currently, adiabatic mode couplers are under investigation and will be reported in future work.

The utilization of thick Si MMWs offers the advantage of accommodating a larger number of modes within a limited area compared to conventional 220-nm-high waveguides, leading to an MDM system with a higher capacity. Furthermore, through the use of grating couplers, certain LP modes from few-mode fibers (*e.g.*, the LP_{11b} mode) can be efficiently converted into higher-order vertical modes

(*e.g.*, the TE_{01} mode) within thick Si MMW waveguides. This direct mode conversion is not achievable with conventional 220-nm-high waveguides and enables subsequent integrated-optical processing (see Appendix D). This study paves the way for the manipulation of vertical higher-order modes in thick Si MMWs, opening up new possibilities for various photonic applications.

APPENDIX

A. ADVANTAGES OF THE SURFACE GRATINGS

This appendix highlights the advantages of shallow-etched surface gratings over sidewall gratings. First, shallow-etched surface gratings offer superior control over their performance through the manipulation of etch depth, etched rectangle width (w_g), and importantly, their position. The position of the etched rectangles introduces an additional degree of freedom in the design that is absent in sidewall gratings. To demonstrate the influence of this positional control, we simulated a PICGAC0 (Photonic Integrated Circuit using Grating-Assisted Coupling to the TE_{01} mode). We varied the edge-to-edge spacing (s) from 0 nm to 600 nm, while keeping the other parameters fixed: $\Lambda - l_g = 136.5$ nm, $w_g = 300$ nm, and etch depth $= 40$ nm (see Fig. 8(a)). For each s value, l_g was slightly adjusted around 136 nm to ensure the backward coupling remained centered at a wavelength of 1550 nm. We then calculated the number of periods (N_p) required for a peak backward transmittance exceeding 0.95 as a function of s (Fig. 8(b)). The results show that N_p increases with s, indicating that the coupling efficiency between the TE_{00} and TE_{01} modes can be effectively tuned by adjusting s. Consequently, both w_g and s can be independently configured to achieve a desired spectral response.

Next, shallow-etched surface gratings can be simultaneously employed with sidewall gratings to generate two independent couplings to different modes. To illustrate this capability, we simulated a PICGAC0 incorporating both grating types. As depicted in Fig. 8(c), the sidewall grating for backward coupling to the TE_{10} mode was designed with alternating sidewall trenches of 50 nm depth. In the EME (eigenmode expansion) solver simulation, the lengths of the regions with trenches were set to $\Lambda - l_g$ and l_g, respectively. The overall parameters were $\Lambda = 272$ nm, $l_g = 135.4$ nm, and $w_g = 300$ nm, and $N_p = 650$. We further assumed the Si strip surface was covered by a 50 nm film with a variable refractive index. When the refractive index of this film is 1.45, distinct rejection bands associated with backward couplings to the TE_{01} and TE_{10} modes appear at 1549.85 nm and 1650.4 nm, respectively, in the transmission spectrum of the PICGAC0 (Fig. 8(d)). Upon increasing the refractive index from 1.45 to 1.65, these bands red-shift by 1.4 nm and 0.6 nm, respectively. Notably, the backward coupling to the TE_{10} mode exhibits less sensitivity to the refractive index change, primarily because its characteristics are governed by the sidewall grating. This dual-coupling capability, with differential sensitivity, could be highly beneficial for

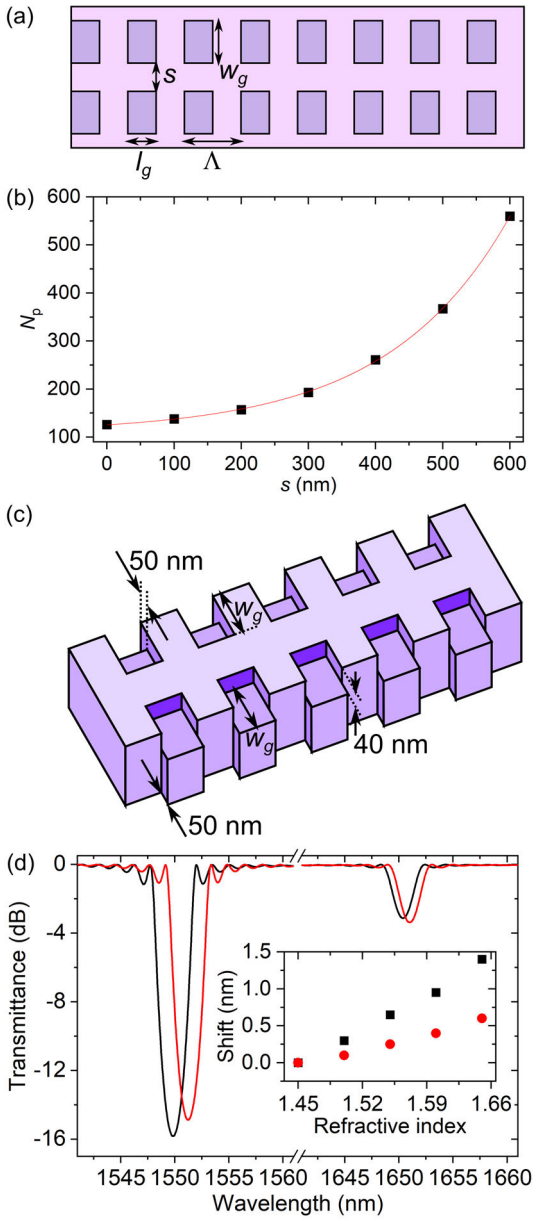

FIGURE 8. (a) Schematic of a shallow-etched grating, illustrating pairs of etched rectangles with a variable edge-to-edge spacing. (b) Number of periods (N_p) required for a peak backward transmittance exceeding 0.95 as a function of s. (c) Schematic of a multimode waveguide (MMW), integrating shallow-etched and sidewall gratings, with its Si strip covered by a 50-nm-thick film of variable refractive index. (d) Transmission spectra of the PICGAC0, comparing results for film refractive indices of 1.45 (black line) and 1.65 (red line). The inset demonstrates the relationship between the wavelength shifts of the transmission dips and the film's refractive index.

applications such as chemical or biological sensing, including temperature detection [23].

Finally, shallow-etched surface gratings are more advantageous than sidewall gratings for coupling to vertical higher-order modes from a fabrication perspective. For efficient coupling to the TE_{01} mode, sidewall trenches would ideally require a vertical length shorter than half the Si strip thickness. This is due to the TE_{01} mode's field node

occurring along the central horizontal line of the waveguide. Consequently, a sidewall grating designed for TE_{01} coupling inherently becomes a surface grating composed of narrow, deeply etched rectangles. For instance, a PICGAC0 with $w_g = 150$ nm and a deep rectangle etch depth of 230 nm exhibits approximately the same rejection band as a PICGAC0 with $w_g = 300$ nm and a shallow rectangle etch depth of 40 nm. Therefore, surface gratings present a significant advantage over sidewall gratings, as they necessitate a considerably smaller etching depth for comparable performance, simplifying fabrication processes.

B. SIMULATION METHOD

All simulations were performed using the EME Solver within Ansys Lumerical Mode. The simulation domain perpendicular to the propagation direction measured 10 μm × 10 μm, with perfectly matched layer (PML) boundaries applied to absorb outgoing waves. A mesh size of 50 nm was used for the region outside the Si strip, while finer meshes of 5 nm were employed within the Si strip. A total of 20 modes were included in the eigenmode expansion, and the 'conserve energy' option was enabled for all EME simulations.

The coupler connecting the single-mode waveguide (SMW) and the multimode waveguide (MMW) within the PICGAC (Photonic Integrated Circuit with Grating-Assisted Coupling) was simulated independently. The slab and strip width transition regions of the coupler were each divided into 20 cells, utilizing the continuously varying cross-sectional subcell (CVCS) method. EME simulations of this coupler revealed a transmittance from the TE_{01} (TE_{11}) mode of the MMW to the TE_{00} mode of the SMW of −28.6 dB (< −100 dB). These results confirm that the couplers introduce negligible influence on the performance of the PICGAC. Consequently, subsequent simulations focused solely on the MMW section incorporating the grating, simplifying the computational domain without compromising accuracy.

C. FWHM EXPRESSION

The FWHM expression for forward coupling is well known [24]. Here, we derive the FWHM expression for backward coupling. The transmittance (T) from one mode to the other mode coupled contra-directionally to the mode is expressed by

$$T = \frac{\kappa^2 \tanh^2(sL)}{s^2 + (\Delta\beta/2)^2 \tanh^2(sL)}, \tag{2}$$

where κ and L represent the coupling coefficient between the modes and a coupling length, equal to $N_p\Lambda$, respectively [25]. $\Delta\beta$ is defined as $2\pi[(n_1 + n_2)/\lambda - 1/\Lambda]$, where n_1 and n_2 represent the effective indices of the modes, and s is defined as $\sqrt{\kappa^2 - (\Delta\beta/2)^2}$. κ is determined by the overlap integral between the two modes over the grating's index perturbation region. $\Delta\beta$ is determined by the dispersions of the two modes.

At λ_c, $\Delta\beta = 0$, and the maximum transmittance is $T = \tanh^2(\kappa L)$, which increases with the product κL. $T = 0.95$ if $\kappa L = 2.178$. At the wavelength $\lambda_c + \delta\lambda$ for which $T = 0.95/2$,

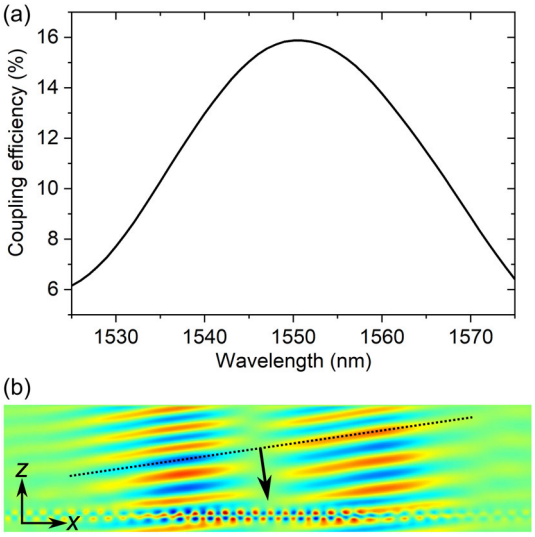

FIGURE 9. (a) Coupling efficiency of a grating coupler, converting the LP_{11b} mode of a step-index fiber into the TE_{01} mode of a 15-μm-wide, 500-nm-thick Si strip waveguide. (b) Distribution of the real part of the electric field's y component at the peak wavelength.

(2) becomes

$$1 - x^2 = \left(x^2 - 2.105\right) \tan^2\left(2.178\sqrt{x^2 - 1}\right), \tag{3}$$

where x is defined as $\Delta\beta/(2\kappa) = 0.2296\Delta\beta L$. The root of (3) is $x = 1.3705$. Because $\Delta\beta$ at $\lambda_c + \delta\lambda$ is expressed by

$$\Delta\beta = \frac{2\pi}{\lambda_c \Lambda}\left[\Lambda\left(\frac{dn_1}{d\lambda} + \frac{dn_2}{d\lambda}\right) - 1\right]\delta\lambda, \tag{4}$$

the FWHM, equal to $2\delta\lambda$, is determined by

$$\mathrm{FWHM} = 1.901\frac{\lambda_c}{N_p}\left|\Lambda\left(\frac{dn_1}{d\lambda} + \frac{dn_2}{d\lambda}\right) - 1\right|^{-1}. \tag{5}$$

As the derivative of $\Delta\beta$ with respect to λ increases, the FWHM decreases. Because κN_p is constant, the FWHM increases with κ.

D. CONVERSION OF LP_{11b} MODE INTO TE_{01} MODE THROUGH GRATING COUPLER

We designed a one-dimensional uniform grating coupler optimized for the transformation of the LP_{11b} mode from a step-index fiber into the TE_{01} mode of a Si strip waveguide. The waveguide possessed dimensions of 500 nm thickness and 15 μm width. The LP_{11b} mode was incident on the grating coupler at an angle of 10°. The grating parameters were designed as follows: an etch depth of 80 nm, a period of 659 nm, and a 50% duty cycle. Fig. 9 illustrates the simulated coupling efficiency from the LP_{11b} mode to the TE_{01} mode, alongside the corresponding electric field distribution at the peak coupling wavelength. It is anticipated that the implementation of nonuniform grating couplers could further enhance the current peak coupling efficiency of 15.9%.

REFERENCES

[1] N. C. Harris, D. Bunandar, M. Pant, G. R. Steinbrecher, J. Mower, M. Prabhu, T. Baehr-Jones, M. Hochberg, and D. Englund, "Large-scale quantum photonic circuits in silicon," *Nanophotonics*, vol. 5, no. 3, pp. 456–468, Aug. 2016.
[2] M. A. Al-Qadasi, L. Chrostowski, B. J. Shastri, and S. Shekhar, "Scaling up silicon photonic-based accelerators: Challenges and opportunities," *APL Photon.*, vol. 7, no. 2, Feb. 2022, Art. no. 020902.
[3] C. Li, D. Liu, and D. Dai, "Multimode silicon photonics," *Nanophotonics*, vol. 8, no. 2, pp. 227–247, Jan. 2019.
[4] S. Hong, L. Zhang, Y. Wang, M. Zhang, Y. Xie, and D. Dai, "Ultralow-loss compact silicon photonic waveguide spirals and delay lines," *Photon. Res.*, vol. 10, no. 1, pp. 1–7, 2022.
[5] A. Rizzo, U. D. Dave, A. Novick, A. P. Freitas, S. P. Roberts, A. James, M. Lipson, and K. Bergman, "Fabrication-robust silicon photonic devices in standard sub-micron silicon-on-insulator processes," *Opt. Lett.*, vol. 48, no. 2, p. 215, 2022.
[6] L.-W. Luo, N. Ophir, C. P. Chen, L. H. Gabrielli, C. B. Poitras, K. Bergmen, and M. Lipson, "WDM-compatible mode-division multiplexing on a silicon chip," *Nature Commun.*, vol. 5, no. 1, p. 3069, Jan. 2014.
[7] X. Wu, C. Huang, K. Xu, C. Shu, and H. K. Tsang, "Mode-division multiplexing for silicon photonic network-on-chip," *J. Lightw. Technol.*, vol. 35, no. 15, pp. 3223–3228, Aug. 1, 2017.
[8] R. Yin, H. Xiao, Y. Jiang, X. Han, P. Zhang, L. Chen, X. Zhou, M. Yuan, G. Ren, A. Mitchell, and Y. Tian, "Integrated WDM-compatible optical mode division multiplexing neural network accelerator," *Optica*, vol. 10, no. 12, pp. 1709–1718, 2023.
[9] S. A. Miller, Y.-C. Chang, C. T. Phare, M. C. Shin, M. Zadka, S. P. Roberts, B. Stern, X. Ji, A. Mohanty, O. A. Jimenez Gordillo, U. D. Dave, and M. Lipson, "Large-scale optical phased array using a low-power multi-pass silicon photonic platform," *Optica*, vol. 7, no. 1, pp. 3–6, 2020.
[10] V. Ginis, I.-C. Benea-Chelmus, J. Lu, M. Piccardo, and F. Capasso, "Resonators with tailored optical path by cascaded-mode conversions," *Nature Commun.*, vol. 14, no. 1, p. 495, Jan. 2023.
[11] S. Signorini, M. Mancinelli, M. Borghi, M. Bernard, M. Ghulinyan, G. Pucker, and L. Pavesi, "Intermodal four-wave mixing in silicon waveguides," *Photon. Res.*, vol. 6, no. 8, pp. 805–814, 2018.
[12] S. Y. Siew, B. Li, F. Gao, H. Y. Zheng, W. Zhang, P. Guo, S. W. Xie, A. Song, B. Dong, L. W. Luo, C. Li, X. Luo, and G.-Q. Lo, "Review of silicon photonics technology and platform development," *J. Lightw. Technol.*, vol. 39, no. 13, pp. 4374–4389, Jul. 15, 2021.
[13] J. L. Pita Ruiz, L. G. Rocha, J. Yang, Ş. E. Kocabaş, M.-J. Li, I. Aldaya, P. Dainese, and L. H. Gabrielli, "Efficient integrated tri-modal coupler for few-mode fibers," *Opt. Exp.*, vol. 30, no. 2, pp. 2539–2546, 2022.
[14] M. M. Milošević, M. Nedeljković, T. M. B. Masaud, E. Jaberansary, H. M. H. Chong, N. G. Emerson, G. T. Reed, and G. Z. Mashanovich, "Silicon waveguides and devices for the mid-infrared," *Appl. Phys. Lett.*, vol. 101, no. 12, 2012, Art. no. 121105.
[15] A. G. Griffith, R. K. W. Lau, J. Cardenas, Y. Okawachi, A. Mohanty, R. Fain, Y. H. D. Lee, M. Yu, C. T. Phare, C. B. Poitras, A. L. Gaeta, and M. Lipson, "Silicon-chip mid-infrared frequency comb generation," *Nature Commun.*, vol. 6, no. 1, p. 6299, Feb. 2015.
[16] M. A. Tran, D. Huang, T. Komljenovic, J. Peters, A. Malik, and J. E. Bowers, "Ultra-low-loss silicon waveguides for heterogeneously integrated silicon/III–V photonics," *Appl. Sci.*, vol. 8, no. 7, p. 1139, Jul. 2018.
[17] D. Huang, M. A. Tran, J. Guo, J. Peters, T. Komljenovic, A. Malik, P. A. Morton, and J. E. Bowers, "High-power sub-kHz linewidth lasers fully integrated on silicon," *Optica*, vol. 6, no. 6, pp. 745–752, 2019.
[18] H. Qiu, J. Jiang, T. Hu, P. Yu, J. Yang, X. Jiang, and H. Yu, "Silicon add-drop filter based on multimode Bragg sidewall gratings and adiabatic couplers," *J. Lightw. Technol.*, vol. 35, no. 9, pp. 1705–1709, May 1, 2017.
[19] S. Paul, M. Kuittinen, M. Roussey, and S. Honkanen, "Multi-wavelength add–drop filter with phase-modulated shifted Bragg grating," *Opt. Lett.*, vol. 43, no. 13, p. 3144, 2018.
[20] X. Wang, H. Yu, H. Qiu, Q. Zhang, Z. Fu, P. Xia, B. Chen, X. Guo, Y. Wang, X. Jiang, and J. Yang, "Hitless and gridless reconfigurable optical add drop (de)multiplexer based on looped waveguide sidewall Bragg gratings on silicon," *Opt. Exp.*, vol. 28, no. 10, pp. 14461–14475, 2020.
[21] Y.-B. Cho, B.-K. Yang, J.-H. Lee, J.-B. Yoon, and S.-Y. Shin, "Silicon photonic wire filter using asymmetric sidewall long-period waveguide grating in a two-mode waveguide," *IEEE Photon. Technol. Lett.*, vol. 20, no. 7, pp. 520–522, Apr. 1, 2008.
[22] K. Y. Yang et al., "Multi-dimensional data transmission using inverse-designed silicon photonics and microcombs," *Nature Commun.*, vol. 13, no. 1, p. 7862, Dec. 2022.
[23] M.-S. Kwon and W. H. Steier, "Microring-resonator-based sensor measuring both the concentration and temperature of a solution," *Opt. Exp.*, vol. 16, no. 13, pp. 9372–9377, 2008.
[24] Q. Liu, Z. Gu, J. S. Kee, and M. K. Park, "Silicon waveguide filter based on cladding modulated anti-symmetric long-period grating," *Opt. Exp.*, vol. 22, no. 24, pp. 29954–29963, 2014.
[25] A. Yariv and P. Yeh, *Photonics: Optical Electronics in Modern Communications* (The Oxford Series in Electrical and Computer Engineering). London, U.K.: Oxford Univ. Press, 2006, pp. 622–626.

HYEONGJUNG KIM received the B.S. degree from Wonkwang University, Iksan, Republic of Korea, in 2024. He is currently pursuing the M.S. degree in electrical engineering with Ulsan National Institute of Science and Technology (UNIST), Ulsan, Republic of Korea. His research interest includes nanophotonic modulators.

JUNGWOO LEE received the B.S. degree from Sejong University, Seoul, Republic of Korea, in 2017. He is currently pursuing the combined master's and Ph.D. degree in electrical engineering with Ulsan National Institute of Technology (UNIST), Ulsan, Republic of Korea. His research interests include integrated photonic devices based on thin-film lithium niobate and silicon-on-insulator platforms.

JIHOON SEO received the B.S. degree from Ulsan National Institute of Science and Technology, Ulsan, Republic of Korea, in 2019, where he is currently pursuing the combined master's and Ph.D. degree in electrical engineering. His research interests include nano-plasmonic and silicon photonic modulators.

MINJIN KIM received the B.S. degree from Ulsan National Institute of Science and Technology (UNIST), Ulsan, Republic of Korea, in 2023, where he is currently pursuing the combined master's and Ph.D. degree in electrical engineering. His research interests include thin-film lithium niobate and inverse design.

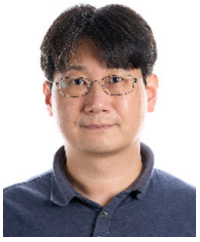

MIN-SUK KWON received the B.S. (summa cum laude), M.S., and Ph.D. degrees in electrical engineering from Korea Advanced Institute of Science and Technology (KAIST), Daejeon, South Korea, in 1998, 2000, and 2005, respectively. He was a Postdoctoral Research Associate with KAIST and the University of Southern California. In September 2007, he joined the Department of Optical Engineering, Sejong University as a full-time Lecturer. In March 2009, he became an Assistant Professor and worked there until January 2012. Since January 2012, he has been an Associate Professor with the Department of Electrical Engineering, Ulsan National Institute of Science and Technology (UNIST). He did active researches on thermo-optically induced long-period gratings. He has been studying integrated-optical devices, such as microring resonators, long-period waveguide gratings, silicon photonic waveguide modulators, and photodetectors. In addition, he strongly focuses on development of nanoplasmonic waveguide devices, graphene-based waveguide devices, and graphene plasmon devices working in the mid-infrared.